

CTAB-assisted Cathodic Electrosynthesis of MnO₂ ultra-fine Nanoparticles and Investigation of Their Charge Storage Performance

Mustafa Aghazadeh¹, Mohammad Reza Ganjali^{2,3,*} and Mohammad Ghannadi Maragheh¹

¹ Material and Nuclear Research School, Nuclear Science and Technology Research Institute (NSTRI), P.O. Box 14395-834, Tehran, Iran

² Center of Excellence in Electrochemistry, School of Chemistry, University of Tehran, Tehran, Iran

³ Biosensor Research Center, Endocrinology and Metabolism Molecular-Cellular Sciences Institute, Tehran University of Medical Sciences, Tehran, Iran

*E-mail: ganjali@khayam.ut.ac.ir

Received: 28 February 2017 / Accepted: 20 October 2017 / Published: 16 December 2017

Cathodic electrodeposition of MnO₂ was performed from 0.005M MnCl₂ in the presence of cetyl trimethylammonium bromide (CTAB). The electrosynthesis experiments were done at a simple direct current (DC) mode by applying current density of 0.5 mA cm⁻² and RT conditions. The obtained brown deposit was then calcined at 300°C for 2h to form the final manganese oxide. Thermal behavior of deposited hydroxide was investigated via thermogravimetric data i.e. DSC-TGA. The structural analysis through XRD and FTIR revealed that the prepared MnO₂ is composed of both α and γ phases. Morphological observations by SEM and TEM exhibited that the prepared and final oxide are composed of completely uniform spherical particles with fine sizes of about 10 nm. The charge storage performances of the prepared MnO₂ nanoparticles were measured by cyclic voltammetry and charge-discharge techniques, which revealed that the produced MnO₂ nanoparticles are capable to deliver specific capacitance as high as 232 and 181 F g⁻¹ at current loads of 0.5 and 2 A g⁻¹ and capacity retentions of 91.89% and 88.25% after 2000 cycling at these current loads. The electrochemical data proved the suitability of the manganese oxide fine particle for use in supercapacitor as electrode material.

Keywords: MnO₂; cathodic electrodeposition; Nanoparticles; Charge storage

1. INTRODUCTION

Supercapacitors are one of the electrochemical energy storage and conversion devices which have been widely used in portable electronic products, electric vehicles, and smart electrical grids. The

competency of any energy storage device depends essentially to its electrode materials which can affect its efficiency and the rate of energy conversion [1-5]. Recently, nanostructured metal oxides and hydroxides such as molybdenum oxide [6], nickel hydroxide [7-11], nickel oxide [12-16], cobalt hydroxide [17-20], cobalt oxide [21-23], manganese oxide [24-29], Mn_3O_4 [30,31], and iron oxide [32,33] were selected as electrode materials of supercapacitors due to their longer cycle life and higher energy density. Among these materials, Mn-based oxides have attracted a lot of attention because of more natural abundance, low cost, several crystal structures, high theoretical specific capacitances (SC), and environmental friendliness [34]. Furthermore, MnO_2 has a flexible microstructure which can be used in different energy storages. MnO_2 is naturally available in various crystallographic structures of α , β , γ , δ and λ [34], which are significantly different from each others. The first three structures have one dimensional tunnels, while the δ and λ have two and three dimensional. It can be definitely stated that these differences can cause enormous differences in their electrochemical properties [34-36]. Generally, the SCs of MnO_2 structures are in order of $\alpha \approx \delta > \gamma > \lambda > \beta$. Therefore, the high capacity of α - and γ - MnO_2 makes them potential candidates for electrode materials in supercapacitors [35,36]. Although MnO_2 is theoretically expected to have SCs of 1370 F/g, the experimental values are only in the range of 150–250 F/g [36], which further undergo fast decreases by increased loading. A major reason is the low electrical conductivity and poor cation diffusivity of MnO_2 , which is proved that only porous thin layers are active in the charge storage phenomena [34].

Considerable studies have been conducted on synthesis of MnO_2 nanostructures with specific morphologies like nanorods, nanowires, nanotubes, nanospheres to improve the capacity behavior of Mn oxides. In this work, we report MnO_2 nanoparticles prepared through cathodic deposition from 0.005 M MnCl_2 bath in the presence of cationic surfactant cetyl trimethylammonium bromide (CTAB). Then, their charge storage capability as supercapacitor electrode materials is studied. It should be stated that cathodic electro-synthesis of manganese oxide has been rarely investigated. Also, supercapacitive performance evaluation of MnO_2 fine nanoparticles as electrode materials has been rarely studied [37-40] and application of CTAB-assisted cathodic agent in electro-synthesis has not been reported till now. Furthermore, we have previously reported that cathodic electro-deposition can be an efficient and easy route for the preparation of ultra-fine nanoparticles of metal oxides and hydroxides [41-43]. Based on our experiences, we develop a facile and easy route for the preparation of MnO_2 ultra-fine nanoparticles with sizes about 10 nm with an efficient yield.

2. EXPERIMENTAL SECTION

2.1. Chemicals

$\text{MnCl}_2 \cdot 4\text{H}_2\text{O}$ (Merck), polytetrafluoroethylene (PTFE, Merck), carbon black, cetyl trimethylammonium bromide (CTAB, Sigma-Aldrich) and Na_2SO_4 (Merck) were used as received. All solutions were prepared using water purified by a UHQ Elga System. An aqueous solution of 5 mM $\text{MnCl}_2 \cdot 4\text{H}_2\text{O}$ was prepared and used for electrodeposition process.

2.2. Preparation of MnO₂ nanoparticles

Manganese oxide nanoparticles were obtained through a simple two-step process. First, the galvanostatic cathodic electrosynthesis from 0.005 M manganese chloride bath containing 0.5 CMC cetyl trimethylammonium bromide (CTAB) as the surfactant was done and a calcination step was then followed at 300 °C for 2h. The electro-synthesis set-up includes a two-electrode system made from stainless steel (316L) cathode centered between two graphite anodes. The precipitation processes on steel cathode were simply received under a direct current (DC) load of 0.5 mA cm⁻². The process time and electrolyte temperature were 100 min and 25 °C, respectively. A home-made electrochemical workstation system (Potentiostat/Galvanostat, Model: NCF-PGS 2012, Iran) was used as power supply. After precipitation process, the steel sheet was washed several times with deionized water and dried at 80 °C for 2h. Then, the deposits were scraped from the steel sheet and hydroxide powder was obtained. The as-prepared brown powder was calcined at 300 °C for 2h in a dry air atmosphere and final black dry oxide powder was obtained.

2.3. Characterization instruments

The crystal structures of samples were determined by powder X-ray diffraction (XRD, a Phillips PW-1800 diffractometer with a Cu K α radiation ($\lambda=1.5406$ Å) at a scanning rate of 5 degree/min. The FTIR spectra of the samples in the range of 400–4000 cm⁻¹ were obtained using a Bruker Vector 22 Fourier transformed infrared spectroscopy with samples in a KBr wafer at ambient temperature. Each FTIR spectrum was collected after 20 scans at a resolution of 4 cm⁻¹ from 400 to 4000 cm⁻¹. Morphologies of the prepared MnO₂ powder were studied by a scanning electron microscope (SEM, LEO 1455 VP, Oxford, UK, operating voltage 30 kV) and transmission electron microscope (TEM, Zeiss EM 900, accelerating voltage of 80 kV). Thermal behavior analysis were carried out in dry air between room temperature and 600°C at a heating rate of 5 °C min⁻¹ using a thermoanalyzer (STA-1500).

2.4. Electrochemical measurements

The working electrode was fabricated by mixing the manganese oxide nanoparticle powder (85 wt.%), carbon black (10 wt.%) and polytetrafluorene ethylene (PTFE, 5 wt.%). A small amount of ethanol was added to the mixture to produce a homogeneous paste. The mixture was then pressed onto steel grid (0.5 cm * 0.5 cm) current collectors to make working electrode, which were used as capacitor electrode to evaluate its charge storage by CV and GCD tests. The electrochemical characterizations were carried out in a conventional three electrode cell containing 1 M Na₂SO₄ as the electrolyte. Platinum wire and Ag/AgCl (saturated with 1 M KCl) electrode were used as the counter and reference electrodes, respectively. All electrochemical tests were provided using an electrochemical workstation system (AUTOLAB[®], Eco Chemie, PGSTAT 30). The CV profiles were taken within the voltage range of 0 - 0.9 V versus Ag/AgCl with applying the potential sweep rates of

5, 10, 20, 50 and 100 mV s⁻¹. The constant GCD tests were carried out at different current loads of 0.5, 1, 2, 4, 7 and 10 A g⁻¹ within a potential range of 0 to 0.9 V versus Ag/AgCl reference electrode.

3. RESULTS AND DISCUSSION

3.1. Heat-treatment and oxide formation mechanism

The deposited hydroxide film was scraped from the steel cathode and the as-obtained powder was calcined at temperature of 300°C for 3h. The structural changes during the calcination process were studied by thermogravimetric (DSC-TG) analysis and the results are presented in Fig. 1.

The DSC curve has a main sharp peak at about 244°C, which is related to the conversion of hydroxide into the oxide product. The TG curve exhibits three step weight losses as the temperature ranges of 25-150°C, 150-300°C and 300-500°C. The first weight loss (about 2.1wt%) in the TG profile can be ascribed to the removal of the H₂O molecules adsorbed on the hydroxide deposited or intercalated in its structure. The second weight loss (about 14.5wt%) can be assigned at temperature range 150-300 °C can be attributed to the decomposition and removal of CTAB along with the conversion from MnOOH to MnO₂ [44]. Notably XRD pattern of our calcined sample at 300°C (presented in Fig. 2b) confirmed the pure MnO₂ crystal structure. The last weight loss is generally corresponding to conversion from MnO₂ to Mn₂O₃. Furthermore, this last weight loss (about 2.8wt%) on the TG curve at the temperature range of 300-500 °C can be also related to the removal of intercalated anions i.e. chloride ions. There is no weight loss at heating up to 600 °C indicating the complete formation of oxide sample, as confirmed by XRD analysis (Fig. 2b). TG curve exhibited total weight loss of 19.4% during heating.

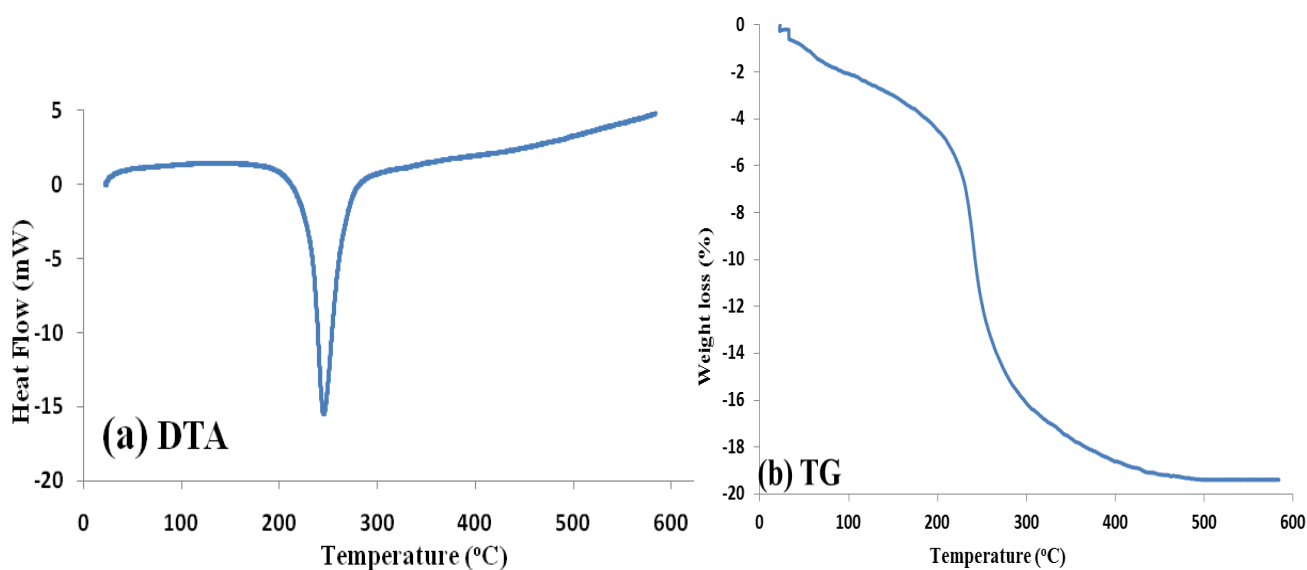


Figure 1. Thermogravimetric analysis of the deposited hydroxide

3.2. Structural and Morphological Characterizations

3.2.1. XRD

The XRD patterns of the electrodeposited and calcined samples are shown in Fig. 2. The as-deposited sample show weak, broad peaks indicating a partially small degree of crystallization and a typical amorphous structure. However, all diffraction peaks at XRD pattern (Fig. 2a) of as deposited sample can be assigned to the manganese oxyhydroxide crystal structure. For the oxide sample, all the diffraction peaks are fully matched with diffraction peaks of α -MnO₂ (JCPDS 44-0141) and γ -MnO₂ (JCPDS 44-0142), as indicated in Fig. 2b. It can be said that our oxide product has both α and γ phases in its composition.

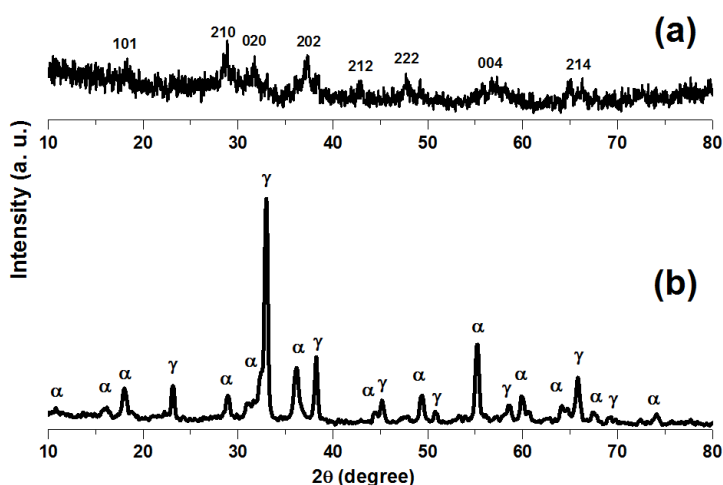


Figure 2. XRD patterns of (a) the electrodeposited sample and (b) calcined at 300 °C for 2h

Manganese oxide has basic MnO₆ octahedral units, which are connected in several paths to produce different crystallographic forms [27,34]. The structure of alpha phase of MnO₂ composed of double chains of edge-sharing MnO₆ octahedral, which are connected at corners to form one-dimensional (2*2) and (1*1) tunnels that expanded in a direction parallel to the *c* axis of the tetragonal unit cell [27]. The size of the (2*2) tunnel is about 4.6 Å, which is suitable for insertion/extraction of Na⁺ cations, especially in charge storage performance in Na₂SO₄ electrolyte. The gamma phase structure is composed a random intergrowth of ramsdellite (2*1) and pyrolusite (1*1) domains [34], which have proper characters for charge storage.

3.2.2. Morphological observations

Figs. 5 and 6 present the SEM and TEM images of the as-deposited hydroxide precursor and the calcined oxide product, respectively. For as- prepared hydroxide powder, a particle texture with regular uniform arrangement and size are seen in SEM images (Figs. 3a and b). The hydroxide particles have mean size of about 10nm. For the calcined powder, a similar morphology is observed. In fact, the

oxide sample has uniform particle morphology with size range of about 10 nm. TEM observations (Figs. 4a and b) clearly showed that the both samples have spherical uniform particle with ~8 nm in size.

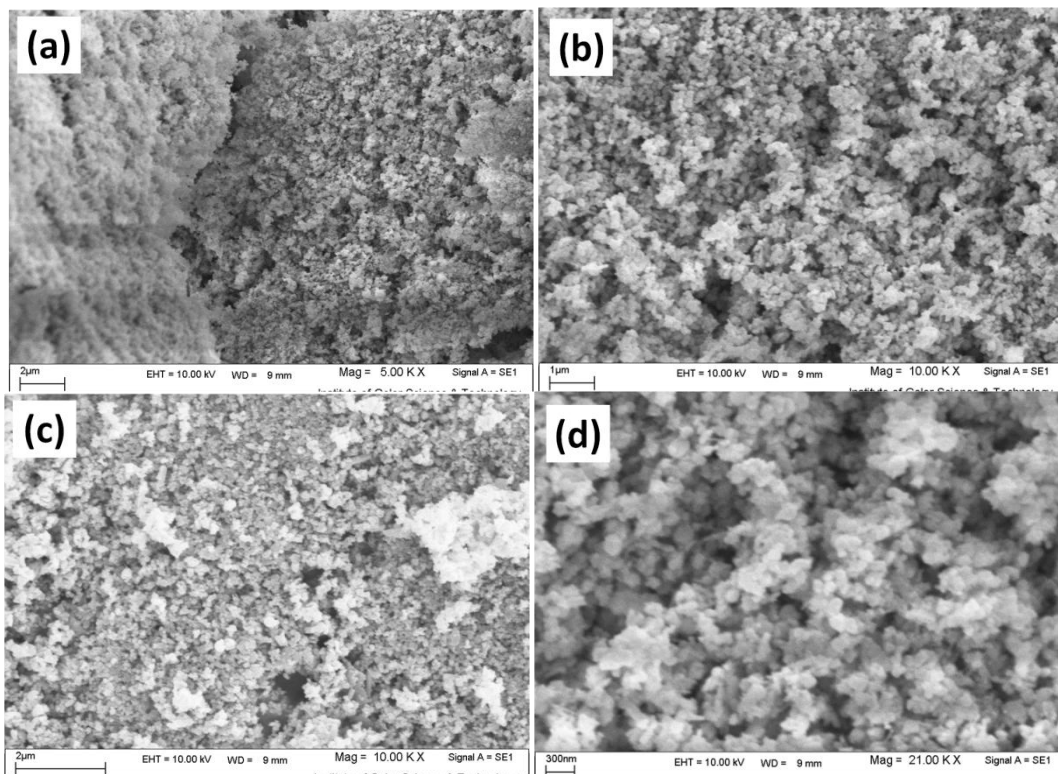


Figure 3. SEM images of (a,b) the electrodeposited and (c,d) calcined samples

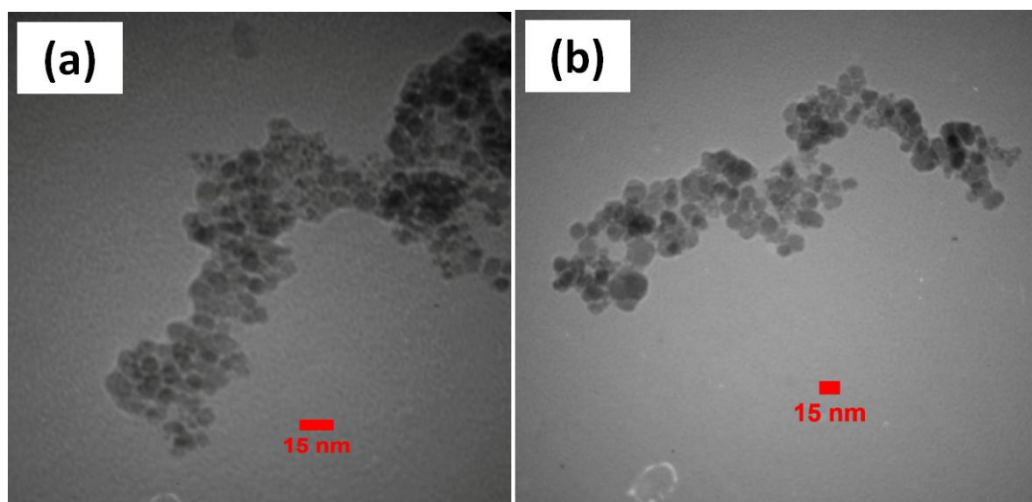


Figure 4. TEM images of (a) the electrodeposited and (b) calcined samples

3.2.3. FT-IR

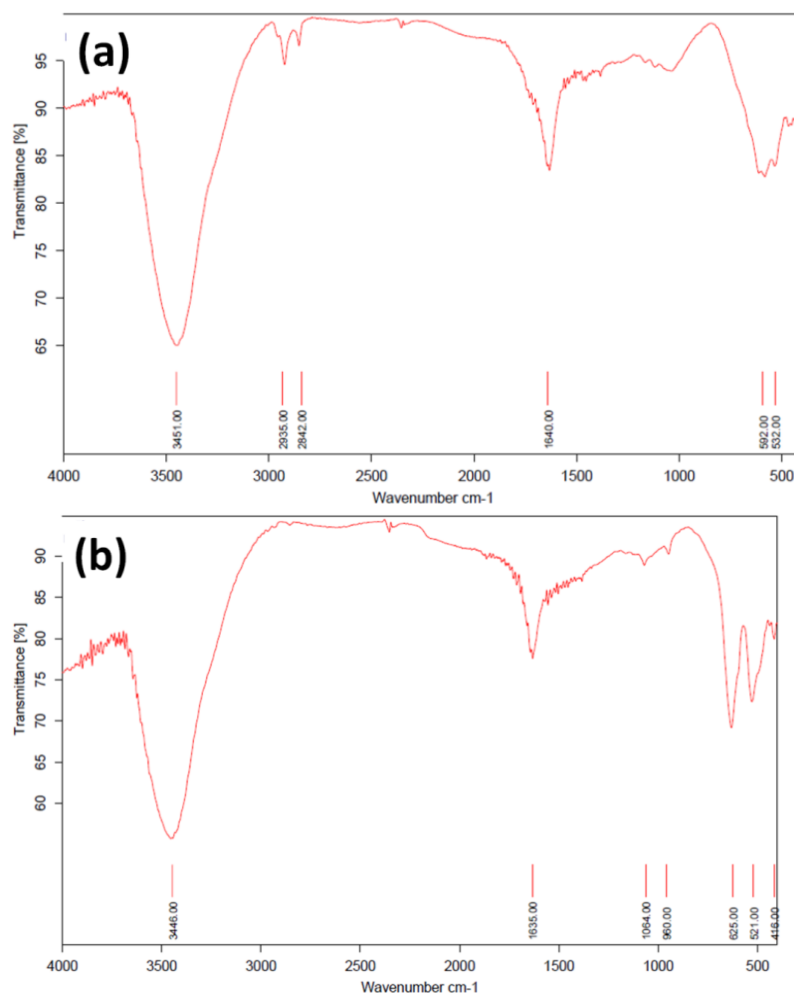


Figure 5. IR spectra of (a) the as-deposited and (b) calcined nanoparticles

Fig. 5 displays the FTIR spectra of the as-prepared and calcined powders. In both spectra, the absorption bands below 700 cm⁻¹ are related to the Mn-O vibration modes [45]. In Fig. 5a, the bands at 592 cm⁻¹, 532 cm⁻¹ and 423 cm⁻¹ can be assigned into the Mn-O-Mn in the MnOOH structure [45]. The peaks at 1078, 1114 and 1139 cm⁻¹ proved the presence of the OH bonds combined with Mn atoms in the forms of γ -OH, δ -2-OH and δ -1-OH, respectively [45,46]. The bands at 3451 and 1640 cm⁻¹ are due to the OH group stretching and water molecule vibrations. Furthermore, several peaks related to the CTAB are seen in the IR spectra of as-deposited powder; the symmetric and asymmetric vibrations of CH₂ at 2935 and 2824 cm⁻¹, respectively, and the peaks at 3009 cm⁻¹, 1487 cm⁻¹, 1354 cm⁻¹, 1281 cm⁻¹, 1105 cm⁻¹, 998 cm⁻¹ are attributed to the asymmetric and symmetric of C-H, C-C stretching, -CH₂ stretching and scissoring vibrations of C-N bounds, respectively [45,46]. In the IR spectrum of oxide sample, the bands at 626, 584, 521 and 416 cm⁻¹ correspond to the Mn-O vibrations in MnO₆ octahedral units of α and γ phases [26-31]. The band at 3446 and 1635 cm⁻¹ are related to the -OH

stretching vibration, and the bands at 1064 and 960 cm^{-1} conventionally correspond to the bending vibrations of $-\text{OH}$ groups [30,31].

3.3. Electrochemical evaluation

3.3.1. Cyclic voltammetry

The prepared MnO_2 nanoparticles were applied as electrode material for supercapacitors and their performances were evaluated by cyclic voltammetry (CV) and galvanostatic charge–discharge (GCD) tests in a 1M Na_2SO_4 aqueous solution. Fig. 6a displays the CV curves of the prepared nanoparticles between 0 and 0.9 V vs. Ag/AgCl at the various scan rates of 2, 5, 10, 20, 50 and 100 mV s^{-1} . All CVs present no peak indicating the charge storage of the fabricated working electrode based on the double layer mechanism. A nearly rectangular shape is also seen at all the applied potential scans implicating the ideal capacitive performance with a fast charge–discharge rate (Fig. 6a).

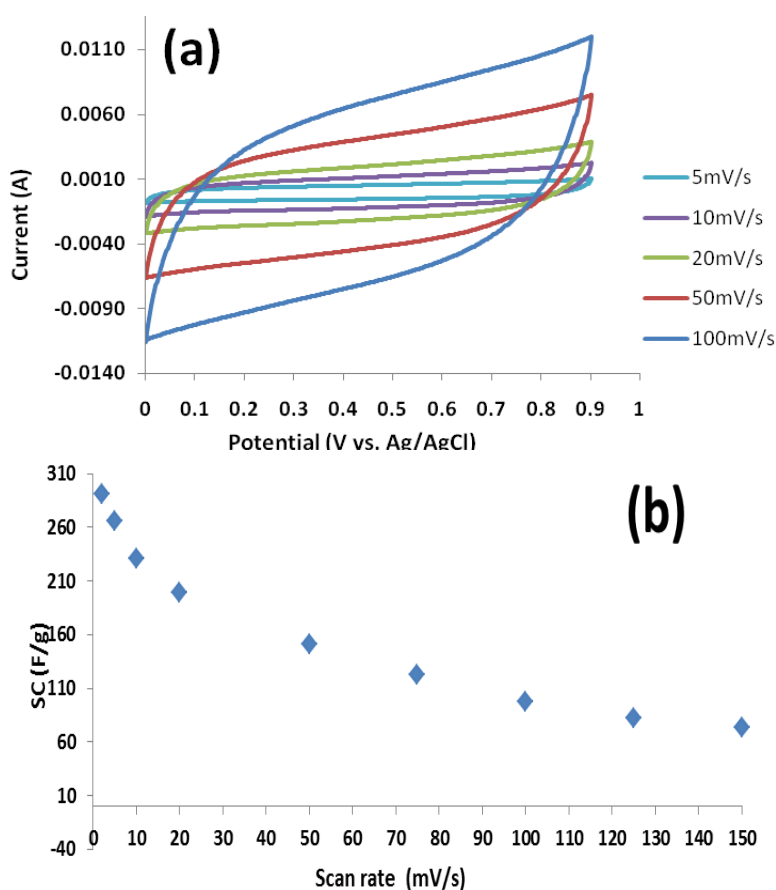


Figure 6. (a) Cyclic voltammograms of the MnO_2 -based electrode at different scan rates from 2-100 mV s^{-1} and (b) calculated capacitance versus scan rate

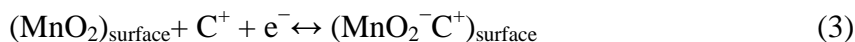
The SCs of the fabricated electrode were determined using following equation:

$$C = \frac{1}{m\nu(\Delta V)} \int_{V_2}^{V_1} I(V) dV \quad (1)$$

where C is the specific capacitance (Fg^{-1}), ΔV is the applied potential window (0.9 V), m is the mass of electroactive material (g), ν is the rate of potential sweep (V s^{-1}), and $I(V)$ is the current response. Using Eq. (1), SCs as high as 291, 266, 231, 199, 151 and 98 F g^{-1} were obtained at the scan rates of 2, 5, 10, 20, 50 and 100 mV s^{-1} , respectively (Fig. 6b). These values proved a proper charge storage ability of the prepared MnO_2 nanoparticles. It was reported that the charge storage in manganese oxide can be explained through two different mechanisms [47]. In one way, intercalation of H^+ or alkali metal cations (e.g. Na^+ , Li^+ , K^+) during reduction followed by deintercalation on oxidation [47].



The second mechanism is related to the surface adsorption of cations on the manganese oxide [48];



As confirmed by XRD data, our prepared MnO_2 had α and γ phase in its composition. The large (2×2) tunnels of α phase facilitates the intercalation/extraction of hydrated Na^+ cations, where the sizes of hydrated Na^+ cations (3.58 Å) are smaller than the tunnel cavities (4.6 Å). On the other hand, the narrow (1×1) tunnels (i.e. 2.3 Å) of γ phase obstacles the intercalation of hydrated Na^+ cations. Hence, the charge storage performance of our prepared MnO_2 nanoparticles is preceded through surface adsorption of cations (Eq. 3).

3.3.2. Charge-discharge tests

The capacitive performance of the fabricated electrode was also investigated by GCD tests. Fig. 7a displays the charge–discharge profiles of the fabricated MnO_2 working electrode at the current loads of 0.2, 0.5, 1, 2 and 4 A g^{-1} . It can be seen that GCD profiles exhibit nearly symmetrical form at all the applied current loads, where the charge curves are similar with their discharge counterparts. Furthermore, the V-t curves exhibit a good linearity, implicating a well-defined capacitive behavior of the prepared MnO_2 nanoparticles. The SCs of the fabricated electrode were calculated based on the discharge curves using Eq. (4) and plotted as a function of current loads as shown in Fig. 7b.

$$C = \frac{I \times \Delta t}{m \times \Delta V} \quad (4)$$

where I is the applied constant current (A), m is the mass of MnO_2 active material, ΔV is the potential window during cycling and Δt is the discharge time of a cycle (s). It was found that the MnO_2 nanoparticles electrode are capable to deliver specific capacitance of 269, 232, 203, 181, 152, 125 and 91 F g^{-1} at the applied current densities of 0.2, 0.5, 1, 2, 4, 7 and 10 A g^{-1} , respectively. These values are in agreements with those calculated based on the CVs (Fig. 5b) and also confirmed a good supercapacitive behavior for the fine particles of MnO_2 .

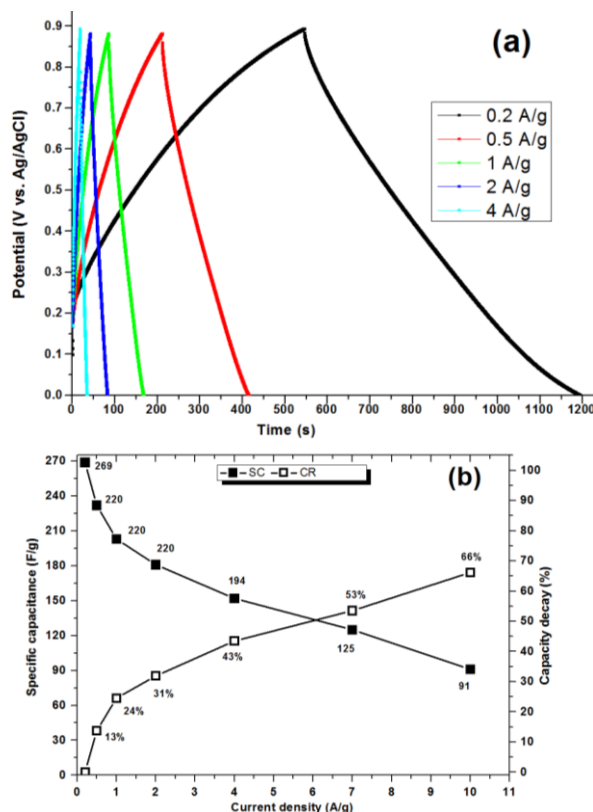


Figure 7. (a) Charge-discharge profiles of the MnO₂ electrode at the different applied current densities, and (b) variation of the specific capacitance vs. applied current density

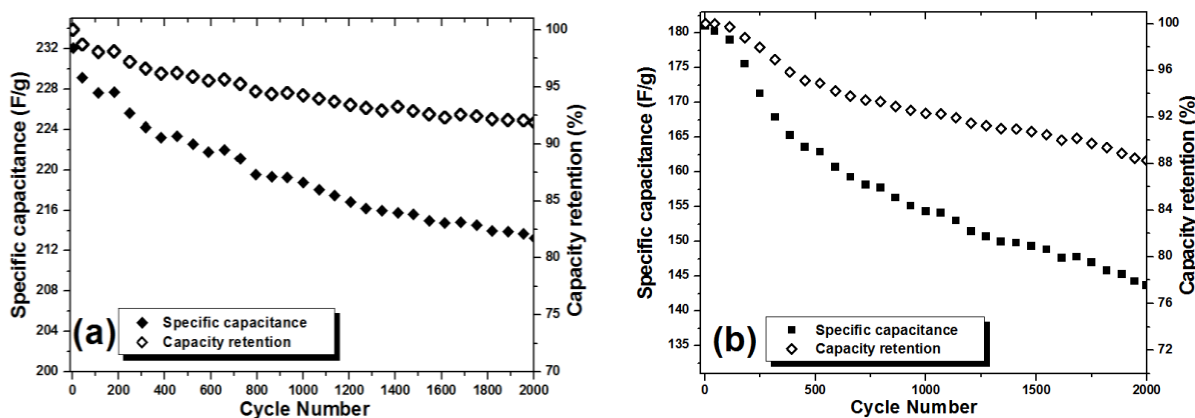


Figure 8. Profiles of specific capacitance capacity retention as a function of the number of GCD cycles at the current loads of (a) 0.5 and (b) 2 A g⁻¹

To evaluate the cycling performance of the fabricated MnO₂ electrode, the continuous GCD tests were carried out at the current loads of 0.5 and 2 A g⁻¹. The variation of SCs as well as capacity retention versus cycle numbers are plotted in Fig. 8. It was observed that the specific capacitance of change from 232 F g⁻¹ to 213.2 F g⁻¹ during continues 2000 GCD cycling at the current load of 0.5 A g⁻¹, which has only 7.21% capacity decay (as seen in Fig. 8a). Also, the fabricated electrode exhibits

88.25% capacity retention after 2000 GCD cycling at the current load of 2 A g^{-1} , and its SC reduces from 181 F g^{-1} to 143.7 F g^{-1} (Fig. 8b). These data confirm the high supercapacitive performance of the prepared manganese oxide nanoparticles.

4. CONCLUSION

Uniform nanoparticles of MnOOH was deposited through cathodic deposition procedure. The calcination of the as-deposited powder at 300°C for 2h resulted fine MnO_2 particles (10 nm) with crystal structure of mixed α and γ phases as confirmed by XRD, SEM and TEM techniques. The CV test resulted the specific capacitance values of 298, 277, 258, 219, 164 and 105 F g^{-1} at scan rates of 2, 5, 10, 20, 50 and 100 mV s^{-1} , respectively. The low capacity decays of 7.21% and 11.75% were observed after 2000 GCD cycling at the current densities of 0.5 and 2 A g^{-1} , respectively. The results of electrochemical evaluations suggest the MnO_2 nanoparticles for use in supercapacitors.

ACKNOWLEDGEMENTS

The authors thank the research council of University of Tehran for financial support of this work.

References

1. X. Zhang, X. Cheng, and Q. Zhang, *J. Energy Chem.*, 25 (2016) 967.
2. J. S. Shayeh, A. Ehsani, M. R. Ganjali, P. Norouzi, and B. Jaleh, *Applied Surface Science* 353 (2015) 594.
3. H. Gholipour-Ranjbar, M. R. Ganjali, P. Norouzi and H. R. Naderi, *Mater. Res. Express* 3 (2016) 075501.
4. K. Adib, M. Rahimi-Nasrabadi, Z. Rezvani, S.M. Pourmortazavi, F Ahmadi, H. R. Naderi, and M. R. Ganjali, *J. Mater. Sci.* 27 (2016) 4541.
5. H. R. Naderi, M. R. Ganjali, A. S. Dezfouli and P. Norouzi, *RSC Advances* 6 (2016) 51211.
6. X. Hu, W. Zhang, X. Liu, Y. Mei, and Y. Huang, *Chem. Soc. Rev.*, 44 (2015) 2376.
7. W. Sun, X. Rui, M. Ulaganathan, S. Madhavi, and Q. Yan, *J. Power Sources*, 295 (2015) 323.
8. M. Aghazadeh, A.N. Golikand, and M. Ghaemi, *Int. J. Hydrogen Energy*, 36 (2011) 8674.
9. M. Aghazadeh, M. Ghaemi, B. Sabour, and S. Dalvand, *J. Solid State Electrochem.*, 18 (2014) 1569.
10. M. Aghazadeh, B. Sabour, M.R. Ganjali, and S. Dalvand, *Appl. Surf. Sci.*, 313 (2014) 581.
11. J. Tizfahm, B. Safibonab, M. Aghazadeh, A. Majdabadi, B. Sabour, and S. Dalvand, *Colloids Surf. A*, 443 (2014) 544.
12. H.Y. Wu, and H.W. Wang, *Int. J. Electrochem. Sci.*, 7 (2012) 4405.
13. L. Junqing, S. Jingli, Y. Xi, Z. Xiaoling, T. Zechao, G. Quanguai, and L. Lang, *Int. J. Electrochem. Sci.*, 7 (2012) 2214.
14. H. Mohammad Shiri, and M. Aghazadeh, *J. Electrochem. Soc.*, 159 (2012) E132.
15. A. Barani, M. Aghazadeh, M.R. Ganjali, B. Sabour, A.A. Malek Barmi, and S. Dalvand, *Mater. Sci. Semicond. Process.*, 23 (2014) 85.
16. M. Aghazadeh, A. Rashidi, M.R. Ganjali, *Int. J. Electrochem. Sci.*, 11 (2016) 11002.
17. M. Aghazadeh, and S. Dalvand, *J. Electrochem. Soc.* 161 (2012) D18.
18. M. Aghazadeh, R. Ahmadi, D. Gharailou, M.R. Ganjali, and P. Norouzi, *J. Mater. Sci.: Mater. Electron.*, 27 (2016) 8623.

19. J.T. Mehrabad, M. Aghazadeh, M.G. Maragheh, M.R. Ganjali, and P. Norouzi, *Mater. Lett.*, 184 (2016) 223.
20. A.A.M. Barmi, M. Aghazadeh, B. Arhami, H.M. Shiri, A.A. Fazl, and E. Jangju, *Chem. Phys. Lett.*, 541 (2012) 65.
21. P. Razmjoo, B. Sabour, S. Dalvand, M. Aghazadeh, and M.R. Ganjali, *J. Electrochem. Soc.*, 161 (2014) D293.
22. M. Aghazadeh, A. Rashidi, and P. Norouzi, *Int. J. Electrochem. Sci.*, 11 (2016) 11016.
23. J. Tizfahm, M. Aghazadeh, M. Ghannadi Maragheh, M.R. Ganjali, P. Norouzi, and F. Faridbod, *Mater. Lett.*, 167 (2016) 153.
24. H. R. Naderi, P. Norouzi and M. R. Ganjali, *Appl. Surf. Sci.*, 366 (2016) 552.
25. M. Aghazadeh, M. Asadi, M. Ghannadi Maragheh, M.R. Ganjali, P. Norouzi, and F. Faridbod, *Appl. Surf. Sci.*, 364 (2016) 726.
26. H. R. Naderi, M. R. Ganjali, and P. Norouzi, *Int. J. Electrochem. Sci.*, 11 (2016) 4267.
27. M. Aghazadeh, M. Ghannadi Maragheh, M.R. Ganjali, P. Norouzi, and F. Faridbod, *Appl. Surf. Sci.*, 364 (2016) 141.
28. M. Aghazadeh, M. Ghannadi Maragheh, M.R. Ganjali, P. Norouzi, D. Gharailou, and F. Faridbod, *J. Mater. Sci.: Mater. Electron.*, 27 (2016) 7707.
29. H. Gholipour-Ranjbar, M. R. Ganjali, P. Norouzi and H.R. Naderi, *J. Mater. Sci. Mater. Electron.*, 27 (2016) 10163.
30. M. Aghazadeh, A. Bahrami-Samani, D. Gharailou, M. Ghannadi Maragheh, M.R. Ganjali, and P. Norouzi, *J. Mater. Sci.: Mater. Electron.*, 27 (2016) 11192.
31. M. Aghazadeh, M. Ghannadi Maragheh, M.R. Ganjali, and P. Norouzi, *RSC Adv.*, 6 (2016) 10442.
32. H. Gholipour-Ranjbar, M.R. Ganjali, P. Norouzi, and H.R. Naderi, *Ceram. Int.*, 42 (2016) 12097.
33. H.R. Naderi, P. Norouzi, M.R. Ganjali, and H. Gholipour-Ranjbar, *Powder Technol.*, 302 (2016) 298.
34. K. Zhang, X. Han, Z. Hu, X. Zhang, Z. Tao, and J. Chen, *Chem. Soc. Rev.*, 44 (2015) 699.
35. J.-G. Wang, F. Kang, and B. Wei, *Prog. Mater. Sci.*, 74 (2015) 51.
36. M. Huang, F. Li, F. Dong, Y. X. Zhang, and L.L. Zhang, *J. Mater. Chem. A*, 3 (2015) 21380.
37. B.G. Sundara Raj, A.M. Asiri, A.H. Qusti, J.J. Wu, and S. Anandan, *Ultrasonics Sonochem.*, 21 (2014) 1933
38. L. Chen, L.J. Sun, F. Luan, Y. Liang, Y. Li, and X.X. Liu, *J. Power Sources*, 195 (2010) 3742.
39. R. Liu, J. Duay, and S. Bok Lee, *ACS Nano*, 4 (2010) 4299.
40. S. Nagamuthu, S. Vijayakumar, and G. Muralidharan, *Ind. Eng. Chem. Res.*, 52 (2013) 18262.
41. R. Cheraghali, M. Aghazadeh, *Anal. Bioanal. Electrochem.*, 8 (2016) 64.
42. I. Karimzadeh, M. Aghazadeh, M.R. Ganjali, P. Norouzi, and S. Shirvani-Arani, *Mater. Lett.*, 179 (2016) 5.
43. M. Aghazadeh, M.G. Maragheh, M.R. Ganjali, and P. Norouzi, *Inorg. Nano-Metal Chem.*, (2017) Doi:10.1080/24701556.2017.1284092.
44. X.D. Sun, and C.L. Ma, *Inorg. Chem. Commun.*, 12 (2002) 747.
45. Z.C. Li, S.S. Chen, C. Dong, X. Hong Chen, Q.F. Zhou, *Micro Nano Lett.*, 8 (2013) 325.
46. W. Zhang, Z. Yang, Y. Liu, *J. Cryst. Growth*, 263 (2004) 394.
47. M. Toupin, T. Brousse, and D. Bélanger, *Chem. Mater.*, 16 (2004) 3184.